

Supplementary Materials for  
**Topologically protected optical polarization singularities in  
four-dimensional space**

Christina M. Spaegle *et al.*

Corresponding authors: Federico Capasso, capasso@seas.harvard.edu;  
Michele Tamagnone, michele.tamagnone@iit.it; Christina M. Spaegle, spaegle@seas.harvard.edu

*Sci. Adv.* **9**, eadh0369 (2023)  
DOI: 10.1126/sciadv.adh0369

**This PDF file includes:**

Supplementary Text  
Figs. S1 to S18  
References

## S1.1 Details on polarization singularities in monochromatic paraxial fields

Polarization singularities in monochromatic paraxial vector fields either require only one or more parameters of the polarization ellipse (e.g., azimuthal angle, ellipticity angle) to be singular or are not topologically protected. The sets of points in 2D for which the polarization azimuth is undefined forms C-points, and the sets of points for which the polarization ellipticity angle is undefined forms L-lines (22). At these C-points and L-lines, the full transverse polarization can still be well-defined; these singular positions are *not complete* polarization singularities. At C-points, light can be perfectly circularly polarized since circular polarization has an undefined azimuth angle. Similarly, along a L-line, light can be perfectly linearly polarized since linear polarization has an undefined ellipticity angle. Such C-points and L-lines are common in random complex paraxial vector fields (22, 30, 31.). In the main paper, the scalar correspondence of speckle fields has been analyzed in detail. As for phase singularities in speckle patterns, small perturbations in the field (e.g., by the addition of stray plane waves) do not destroy C-points and L-lines, but only displace them. Note that this protection is also guaranteed in 3D nonparaxial fields, where C-points and L-lines turn into C-lines and L-lines, respectively. (The fact that L-lines do not turn into surfaces is described in detail in (20) and is based on the fact that for nonparaxial fields 2 conditions need to be fulfilled to ensure an undefined ellipticity angle.).

For V-points and dark C-points, the intensity is zero and the polarization is hence not defined. However, the field in the immediate vicinity of the singularity is polarized in a certain basis (linear and circular, respectively) and will split into multiple bright C-points for, e.g., any elliptically polarized perturbation (8, 56). They are hence not topologically protected.

## S1.2 Degree of a function and winding number

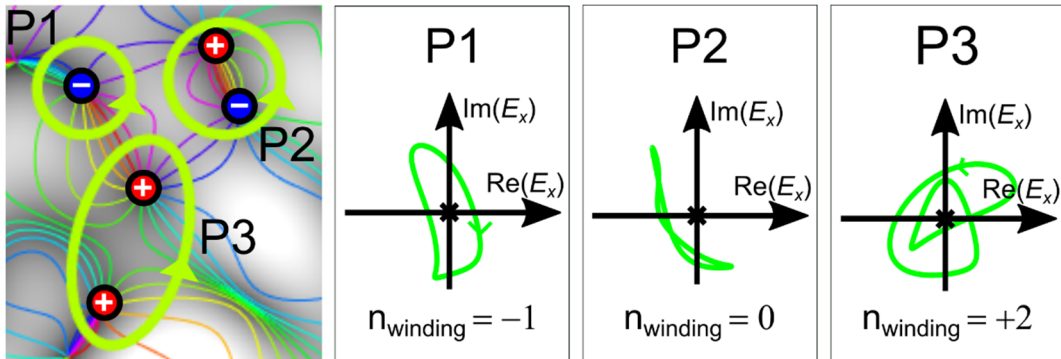


**Figure S1: Winding number and topological charge.** a, Considering a closed path (not self-intersecting or crossing a singularity) on the  $(x, y)$  plane (green curves in left panel), we can map the complex field value of each point on this path to a point in the  $(E_{\Re}, E_{\Im})$  plane (right panels). The number of times the created closed curve winds around the origin in that plane corresponds to the winding number  $w$ , which is the sum of the topological charges of the zero points inside the closed path in the  $(x, y)$  plane.

The winding number represents the total number of times a closed curve rotates around a point. It is a signed quantity, positive for counter-clockwise rotation, negative for clockwise rotation. The curve can have any shape but must be smooth and not crossing through the point of interest or other singular points. In this paper, the curve lies in the  $(E_{\Re}, E_{\Im})$  plane, with  $E_{\Re}$  and  $E_{\Im}$  being the real and imaginary part of the field, and the point of interest is the origin. (Figure S1 left panel). The curve is created by choosing a closed path in the  $xy$  plane of the modelled field on a 2D screen (Figure S1 left panel) and plotting the field value

at each position of the curve in the  $(E_{\Re}, E_{\Im})$  plane (Figure S1 right panel). The closed path in the  $xy$  plane is hence not allowed to go through a singularity, as it would correspond to the curve crossing the origin in the  $(E_{\Re}, E_{\Im})$  plane. The winding number is then calculated by

$$w = \frac{1}{2\pi} \oint_P \frac{E_{\Re} dE_{\Im} - E_{\Im} dE_{\Re}}{E_{\Re}^2 + E_{\Im}^2} \quad (\text{S1})$$

Intuitively, this equation integrates over a change in polar angle  $\theta = \arctan\left(\frac{E_{\Im}}{E_{\Re}}\right)$ . As the loop is closed, the overall rotation angle will be a multiple of  $2\pi$  so that the field returns to the starting complex value. Under continuous deformation this number is constant because it can be only changed when the loop crosses the singularity point which is not allowed by definition. The winding number is hence a topological invariant under continuous deformations and/or perturbations of the field as long as the curve does not cross a singularity. Formally, this means that for sufficiently small perturbations the winding number is an integer constant.

The field of differential topology provides an immediate generalization for higher dimensions. The winding number is defined for 1D paths in 2D plane  $\mathbb{R}^2$ , while the degree is valid for the more general case  $\mathbb{R}^n$  (36). To understand how the generalization works we notice that in the case of the winding number, one can see the path  $P$  as a smooth function (*diffeomorphism*) from one circumference to another. The first circumference is identified by a parameter  $s$  in the range  $[0, 2\pi]$  which is used to define the closed path  $P$  in the parametric form  $P(s)$ , such that  $P(0) = P(2\pi)$ . The second circumference is simply the polar angle (which we assume to be always well defined as discussed earlier) also in the range  $[0, 2\pi]$ . Then we can identify a function  $f: s \rightarrow \theta$  and the winding number is simply how many times this function wraps around in  $\theta$ , with the sign identifying the direction. Practically, this can be achieved with the integral in equation (22) or by taking a regular value  $\theta_0$  (i.e., any value for which  $f'$  is not zero) and finding all the values  $\{s_1, s_2, \dots\}$  which map to it, so that  $f(s_i) = \theta_0$ ; at each  $s_i$  the function can have either positive derivative (counter-clockwise motion) or negative derivative (clockwise motion), and the difference of the number of points for which it is clockwise and the ones for which it is counter-clockwise is the winding number.

Importantly, the points  $0$  and  $2\pi$  have been glued together in both ranges, so that the topology is the non-trivial one of a circumference, also called a *1-sphere*. An *n-sphere*  $S^n$  in differential topology is defined as the set of points in a  $n+1$  dimensional space which have a distance equal to 1 from the origin. For  $n=1$  it is a circumference in the plane, for  $n=2$  is a spherical surface in the space and so on in higher dimensions. The degree in higher dimensions (in our case we use the case  $n=3$  for a 3-sphere that defines our topological invariant in 4D) is defined similarly to the winding number: starting from the function  $f: S^n \rightarrow S^n$  we consider a regular value  $p$  in the co-domain and the points  $\{s_1, s_2, \dots\}$  which map to it. The derivative is now replaced by the local Jacobian which can be inverting (negative determinant) or non-inverting (positive determinant). The number of points with non-inverting Jacobian minus the number of points with inverting Jacobian is the degree.

The Jacobian is intimately related to this topological invariant: we use here the Jacobian of the function between n-spheres, which depends on the Jacobian of the fields (in the  $n+1$  space).

## Calculating the topological degree by integrating over the 3D hypersphere in 4D space

The charge of the singularity is indeed a topological invariant, which can be either determined by  $m_{4D} = \text{sign}(\det(\bar{J}))$  at the singularity position as described in the main paper or computed with an integral over a three-dimensional hypersphere, that wraps around the singularity in 4D space:

The topological charge is simply defined as the degree of the function  $\mathbf{E}: \mathbb{R}^4 \rightarrow \mathbb{R}^4$  from  $(x, y, z, \lambda)$  to  $(E_{x\Re}, E_{x\Im}, E_{y\Re}, E_{y\Im})$  evaluated on a closed surface  $S$  around a zero. The surface must not intersect any other zero. Therefore, we can normalize  $\mathbf{E}$  by dividing by its norm:  $\hat{\mathbf{E}} = \frac{\mathbf{E}}{|\mathbf{E}|}$ .

We now consider the surface  $S$  and its image  $\hat{\Gamma}$  through the function  $\hat{\mathbf{E}}$  (Figure S2). Due to the normalization of  $\hat{\mathbf{E}}$ , the image  $\hat{\Gamma}$  lies on a  $S_3$  unit hypersphere. More intuitively, normalizing is equivalent to radially project point by point the closed manifold  $\Gamma$  on the unit hypersphere  $\hat{\Gamma}$ . If  $\hat{\Gamma}$  wraps around the origin  $n$ -times, its “surface” corresponds to  $n * 2 \pi^2$  and the degree  $D = n$ . The number of wrappings can be evaluated integrating a differential of  $\hat{\mathbf{E}}$  and dividing by the surface area  $2 \pi^2$  (similar to the 2D integral in Equation S1). We will derive and evaluate this integral over the 3D hypersphere numerically, which will lead as expected to the topological charge identical to  $m_{2D} = \text{sign}(\det(\bar{\mathbf{J}}))$ , i.e.  $D=-1$  for the singularity presented in the main paper:

The integral can be done meshing  $S$ , which is accomplished establishing a 3-dimensional coordinates system on it. For instance, if  $S$  is itself a hypersphere, this can be achieved simply with hyperspherical coordinates that naturally generalize spherical coordinates. If not, then a simple diffeomorphism can be used to apply hyperspherical coordinates to  $S$ . The differentials along each of the coordinates (let’s call them  $\alpha, \beta, \gamma$ ) are mapped by  $\mathbf{E}$  to  $d_\alpha \Gamma, d_\beta \Gamma, d_\gamma \Gamma$ . Differentials in higher dimensional spaces can be represented more easily using *exterior algebra*. Specifically, using the exterior product (also known as wedge product) we can write the expression  $d_\alpha \Gamma \wedge d_\beta \Gamma \wedge d_\gamma \Gamma$  that fully preserves the information about size and orientation of this 3D differential in a 4D space.

Let us now project this differential radially on the unit hypersphere  $\hat{\Gamma}$ . This is equivalent to finding the “hyper solid” angle subtended by the differential  $d_\alpha \Gamma \wedge d_\beta \Gamma \wedge d_\gamma \Gamma$ . Let us call this differential angle  $d^3 \Omega$ . Evaluating the topological degree is then accomplished by completing the integral on all  $\Gamma$  of the solid angle and then dividing by the surface of the unit hypersphere  $\hat{\Gamma}$  (which is  $2 \pi^2$ ):

$$D = \frac{1}{2 \pi^2} \iiint d^3 \Omega \quad (\text{S2})$$

The last step consists in calculating  $d^3 \Omega$ . This can be accomplished by performing an additional exterior product with the unit vector  $\hat{\Gamma} = \frac{\Gamma}{|\Gamma|}$  obtaining  $\hat{\Gamma} \wedge d_\alpha \Gamma \wedge d_\beta \Gamma \wedge d_\gamma \Gamma$  which, as well known from exterior algebra, represents a parallelotope having as edges the four vectors. Since  $\hat{\Gamma}$  is a unit vector, the volume of this parallelotope is equivalent to the surface of its shadow projected on the sphere with radius  $|\Gamma|$ . To find the value on the unit sphere  $\hat{\Gamma}$  we need to further normalize dividing by  $|\Gamma|^3$ . The final differential is then:

$$\frac{\Gamma \wedge d_\alpha \Gamma \wedge d_\beta \Gamma \wedge d_\gamma \Gamma}{|\Gamma|^4} \quad (\text{S3})$$

The volume of this normalized differential is therefore identical to  $d^3 \Omega$ . We can calculate this volume using the determinant of the associated Gram matrix:

$$d^3\Omega = \frac{1}{|\Gamma|^4} \begin{vmatrix} \Gamma_1 & \Gamma_2 & \Gamma_3 & \Gamma_4 \\ d_\alpha \Gamma_1 & d_\alpha \Gamma_2 & d_\alpha \Gamma_3 & d_\alpha \Gamma_4 \\ d_\beta \Gamma_1 & d_\beta \Gamma_2 & d_\beta \Gamma_3 & d_\beta \Gamma_4 \\ d_\gamma \Gamma_1 & d_\gamma \Gamma_2 & d_\gamma \Gamma_3 & d_\gamma \Gamma_4 \end{vmatrix} \quad (S4)$$

Where each row of the matrix represents each vector of the exterior product, written in terms of entries in the 4D codomain space (for simplicity we used 1, 2, 3, 4 to name the dimensions instead of  $E_{x\Re}, E_{x\Im}, E_{y\Re}, E_{y\Im}$ ).

We finally get:

$$D = \frac{1}{2\pi^2} \iiint \frac{1}{|\Gamma|^4} \begin{vmatrix} \Gamma_1 & \Gamma_2 & \Gamma_3 & \Gamma_4 \\ d_\alpha \Gamma_1 & d_\alpha \Gamma_2 & d_\alpha \Gamma_3 & d_\alpha \Gamma_4 \\ d_\beta \Gamma_1 & d_\beta \Gamma_2 & d_\beta \Gamma_3 & d_\beta \Gamma_4 \\ d_\gamma \Gamma_1 & d_\gamma \Gamma_2 & d_\gamma \Gamma_3 & d_\gamma \Gamma_4 \end{vmatrix} \quad (S5)$$

Performing this integral numerically leads as expected to the topological charge identical to  $m_{2D} = \text{sign}(\det(\bar{J}))$ , i.e.  $D=-1$  for the singularity presented in the main paper.

Note that this is the direct generalization of the 2D case:

$$D = \frac{1}{2\pi} \oint \frac{1}{|\Gamma|^2} \begin{vmatrix} \Gamma_1 & \Gamma_2 \\ d_\alpha \Gamma_1 & d_\alpha \Gamma_2 \end{vmatrix} = \frac{1}{2\pi} \oint \frac{\Gamma_1 d_\alpha \Gamma_2 - \Gamma_2 d_\alpha \Gamma_1}{\Gamma_1^2 + \Gamma_2^2} \quad (S6)$$

Which is the well-known expression for the winding number shown in Eq. S1. It is useful to represent this mathematical procedure graphically for this last simpler case (Figure S2).

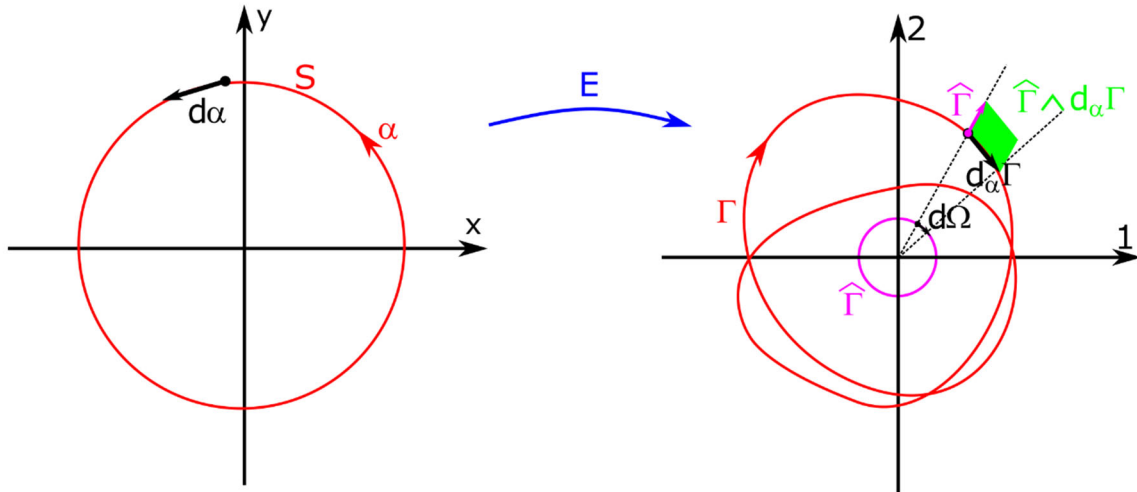


**Figure S2:** Graphical representation of the mathematical procedure to acquire the winding number

### S1.3 Singular value decomposition of the Jacobian

As described in the main paper, the Jacobian can be used to describe the field near the singularity. For the simplest case of a Laguerre-Gaussian beams (with rotational index  $m \neq 0$ ), the Jacobian is the unity matrix (Equation 2), describing a field that is rotationally symmetric in intensity. (Figure S3a). In a more general case, however, the field can be elongated in a certain direction, changing the intensity distribution and the density of the equiphase lines (Figure S3d). The information about the field can be immediately read out of the Jacobian, which can be decomposed into three simple transformations acting on the Laguerre-Gaussian beam profile, using Single Value Decomposition (SVD, Figure S3). Using the SVD, the Jacobian can be written as:

$$J = U \Sigma V^* \quad (S7)$$

where  $V$  corresponds to an initial rotation,  $\Sigma$  to a scaling along the coordination axis and  $U$  to another rotation.

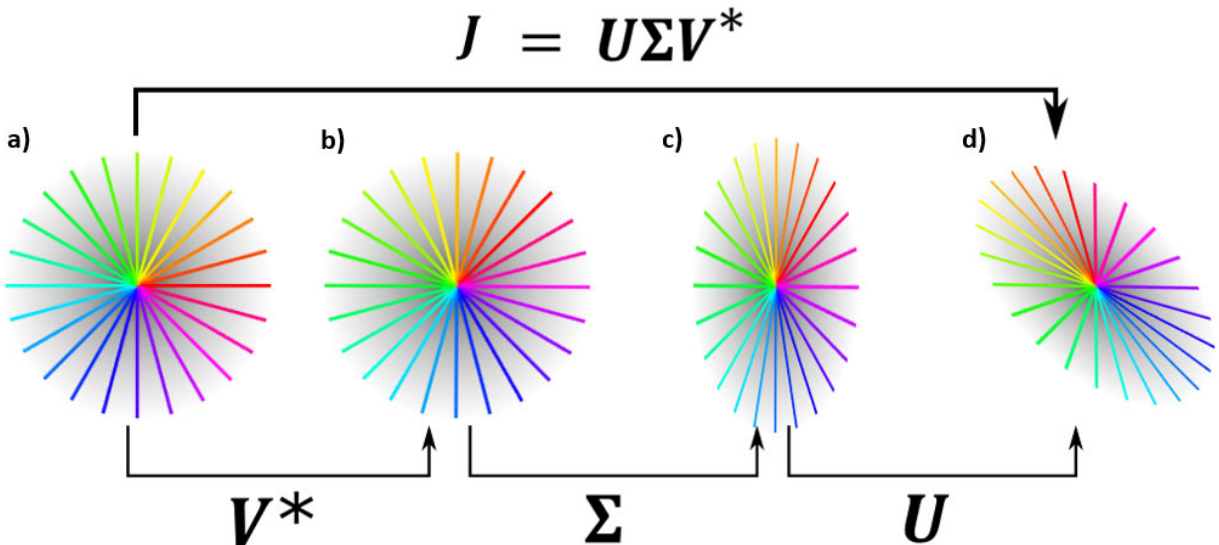


**Figure S3: Singular value decomposition.** The Jacobian  $\bar{J}$  describes the field around the singularity position. In case of a diagonal unitary Jacobian the field has the shape of an ordinary Laguerre gaussian beam (a). For more general cases, the Jacobian can be decomposed into three simple transformations through Singular Value Decomposition i.e., an initial rotation  $V$  (b), a diagonal scaling matrix  $\Sigma$  that scales the profile along the coordination axis (c) and a final rotation matrix  $U$  (d).

The SVD can be used to express the Jacobian by the parameters of the polarization ellipse, namely, the global phase  $\phi$  at the major axis (angle from 0 to  $2\pi$ ), the gradient  $a$  along major axis (real positive), the gradient  $b$  along minor axis (real, sign is topological charge) and the angle  $\theta$  of major axis (angle from 0 to  $2\pi$ ). Then one can write:

$$V^* = \begin{pmatrix} \cos \phi & \sin \phi \\ -\sin \phi & \cos \phi \end{pmatrix}; \quad \Sigma = \begin{pmatrix} a & 0 \\ 0 & b \end{pmatrix}; \quad U = \begin{pmatrix} \cos \theta & -\sin \theta \\ \sin \theta & \cos \theta \end{pmatrix} \quad (S8)$$

and hence

$$\mathbf{M} = \begin{pmatrix} a \cos \theta \cos \phi + b \sin \theta \sin \phi & a \cos \theta \sin \phi - b \sin \theta \cos \phi \\ a \sin \theta \cos \phi - b \cos \theta \sin \phi & a \sin \theta \sin \phi + b \cos \theta \cos \phi \end{pmatrix} \quad (S9)$$

## S1.4 Stationary points in the field and the role of the determinant of the Jacobian

In addition to the phase singularities in the 2D spackle pattern case discussed, it has been pointed out [Michael Berry, private communication, 4<sup>th</sup> July 2022, Erice, Italy] that other special points in the field (such as saddle points in the phase) are also relevant to describe the evolution of singularities when the field is perturbed.

Following a more careful analysis, we noticed that the following points all lie on the yellow lines in Figure 2D formed by the points where  $\det J = 0$ :

- Stationary points (maxima, non-singular minima and saddle points) in intensity
- Stationary points (maxima, minima and saddle points) in the phase
- Stationary points (maxima, minima and saddle points) in the real and imaginary parts of the field

This can be shown mathematically as follows: any real 2X2 matrix  $J$  with  $\det J = 0$  can be written in the following form parametrized by 3 real parameters  $A, B, \theta$ :

$$J = \begin{pmatrix} A \cos \theta & B \cos \theta \\ A \sin \theta & B \sin \theta \end{pmatrix} = \begin{pmatrix} \cos \theta \\ \sin \theta \end{pmatrix} (A \quad B) \quad (\text{S10})$$

This implies that for any small displacement in the  $xy$  plane, the corresponding offset in the complex plane is  $\delta(\cos \theta + i \sin \theta) = \delta e^{i\theta}$  with  $\delta$  some real constant, meaning a complex value in the direction  $\theta$ . If  $\theta$  is 0 or  $\pi/2$  the point is a stationary point for the imaginary and the real part respectively. Considering now the value of the field in the considered point as  $C e^{i\phi}$ , if  $\phi$  and  $\theta$  are parallel directions, then the point is a stationary point in the phase. If they are orthogonal, then the point is a stationary point in the intensity.

## S2 Complete polarization singularity details

### S2.1 Proof that all polarizations exist around the singularity in the 3D space ( $dx, dy, dz$ ) at the design wavelength ( $\Delta\lambda = 0$ )

Using the inverse function argument in the main paper it is trivial to show that in 4D a neighborhood of the singularity all the polarizations and phases exists. However, we can also prove that in the 3D space (without changing the wavelength) all polarizations exist. Let us define the input space  $U$  formed by vectors  $u = (\Delta x, \Delta y, \Delta z, \Delta \lambda)^T$  and the output space  $V$  formed by vectors  $v = (E_{xR}, E_{xI}, E_{yR}, E_{yI})^T$

The Jacobian  $J$  is full rank since its determinant is non-zero, so spanning around  $dx, dy, dz$  gives three linearly independent vectors in the  $V$  space. **It is always possible to combine linearly these three vectors to obtain a  $v$  vector with the last two elements set to 0.** This implies that we can always find a point in the 3D space such that the polarization is horizontal. The same argument holds of course for vertical polarization.

For any other arbitrary desired polarization, we can choose a vector  $v$  which represents that polarization and has all entries different from zero (using the phase degree of freedom). Then, we can always construct a full-rank matrix  $W$  such that  $Wv$  is horizontally polarized (i.e., its last two entries are zero). Physically,  $W$  could for instance represent a waveplate without losses. Mathematically, a possible construction is:

$$W = \begin{pmatrix} E_{x\Re} & 0 & E_{y\Re} & 0 \\ 0 & E_{x\Im} & 0 & E_{y\Im} \\ -E_{y\Re} & 0 & E_{x\Re} & 0 \\ 0 & -E_{y\Im} & 0 & E_{x\Im} \end{pmatrix} \quad (S11)$$

It is easy to verify that the last two entries of  $Wv$  vanish, and the matrix is full rank because the determinant is  $(E_{x\Re}^2 + E_{y\Re}^2)(E_{x\Im}^2 + E_{y\Im}^2)$  which is greater than zero because no entry is zero.

Let us then consider the matrix  $WJ$ : we can apply the same argument as above and find a point  $u$  in the  $U$  space such that the  $WJu$  is horizontally polarized, which means that  $W^{-1}WJu = Ju$  is the desired polarization. We then conclude that for any desired arbitrary polarization we can find a point in space with that polarization. However, the phase cannot be controlled: only accessing the full 4D  $U$  space it is possible to find all the polarizations *and* phases.

This method works because both matrices  $J$  and  $W$  have full rank.  $W$  has full rank because it has no losses, and therefore the product  $WJ$  has full rank because the determinant of  $WJ$  is the product of determinants which are both non-zero.

## S2.2 Polarization distribution around the singularity

As shown in Figure b in the main paper, one can find all polarizations twice on a surface of equal intensity around the singularity. Figure S4 shows the relation between the  $z$  position on this surface (a) and the position on the Poincare sphere (b). Figure S4 shows that one can indeed find all polarizations around the singularity, as the Poincare sphere is fully covered when mapping the simulated polarization states of an ellipsoid of constant intensity around the singularity onto the Poincare sphere.

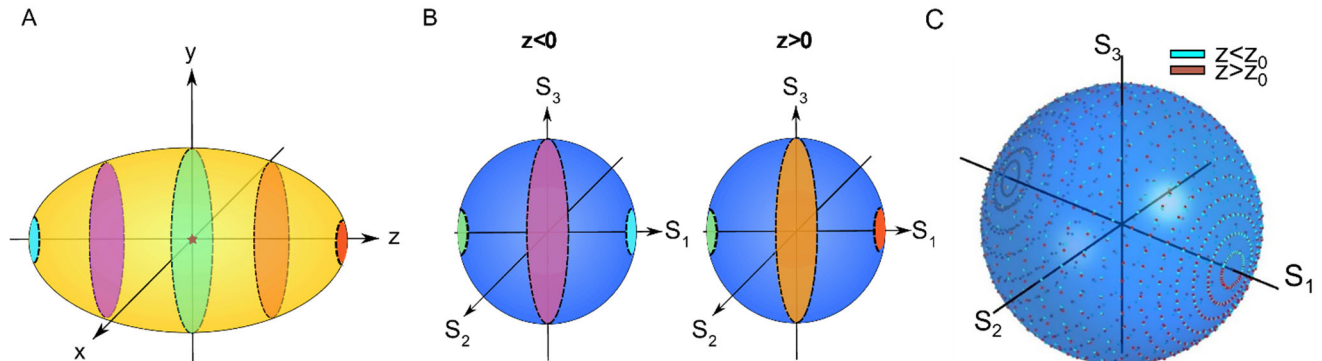


**Figure S4. 3D space mapping to Poincare sphere.** **a**, Schematic of a surface around the singularity position (star at the origin) of equal intensity. xy-planes located at different  $z$  positions are marked in different colors, assuming the singularity is positioned at  $(x,y,z,\lambda)=(0,0,0,\lambda_0)$ . **b**, Poincare sphere for  $z$  larger and smaller than zero. It shows that each point on the Poincare sphere is crossed twice when the polarization states on the surface in a) are mapped onto the Poincare sphere. **c**, Simulated polarization on ellipsoid surface (axis  $l_x = l_y = 0.3\mu m$ ,  $l_z = 10\mu m$ ) of equal intensity plotted on the Poincare sphere.

## **S2.3 Paraxiality of the system**

In paraxial or weakly-focused optics, the longitudinal field can be ignored to an excellent degree of approximation(1). Our system is firmly in the paraxial regime with a focusing NA of only 0.08.

We would further like to point out that it is always possible to arbitrarily approach the paraxial configuration for any non-paraxial system adding achromatic lenses, as the topological singularity is invariant to this transformation (as long as the system does not crop the beam reducing its etendue). This can be seen easiest in the ray picture: As described in the paper the metasurface acts as a spatially varying waveplate that converts the impinging linearly polarized light into different polarizations (Figure 2C), with the characteristic that each point of the field right after the metasurface has a different polarization except for one counterpart of equal polarization but opposite sign. This leads to destructive interference at the focal position of the lens, since these two polarization states have the same optical path length to the focal position. The metasurface additionally controls the dispersion behavior so that this destructive interference is achieved at one wavelength only. When adding an additional achromatic thin lens concentric with the metasurface-lens system, each pair of opposite polarization state will still have the same (overall increased or decreased) optical path length, leading to destructive interference at the focal position. As the lens is achromatic, the overall chromatic dispersion won't be changed, hence ensuring the existence of the singularity in 4D space.

## **S3 Metasurface design and simulation details**

### **S3.1 Change of basis between Equations 4 and 6**

Starting from Equation 4 in the main paper

$$\mathbf{dE} = \begin{pmatrix} E_{x\Re} \\ E_{x\Im} \\ E_{y\Re} \\ E_{y\Im} \end{pmatrix} = \bar{\mathbf{J}} \begin{pmatrix} dx \\ dy \\ dz \\ d\lambda \end{pmatrix} = J_0 \begin{pmatrix} 1 & 0 & 0 & J_{14} \\ 0 & 1 & 0 & J_{24} \\ 0 & 0 & 1 & J_{34} \\ J_{41} & J_{42} & J_{43} & J_{44} \end{pmatrix} \begin{pmatrix} dx \\ dy \\ dz \\ 0 \end{pmatrix} = J_0 \begin{pmatrix} dx \\ dy \\ dz \\ 0 \end{pmatrix}$$

we can express the field as a Jones vector

$$\begin{aligned} |\mathbf{d}\psi\rangle &= \begin{pmatrix} E_{x\Re} + iE_{x\Im} \\ E_{y\Re} + iE_{y\Im} \end{pmatrix} = J_0 \begin{pmatrix} dx + idy \\ dz \end{pmatrix} = J_0 \left[ (dx + idy) \begin{pmatrix} 1 \\ 0 \end{pmatrix} + dz \begin{pmatrix} 0 \\ 1 \end{pmatrix} \right] \\ &= J_0 [(dx + idy)|\mathbf{H}\rangle + dz|\mathbf{V}\rangle] \end{aligned} \quad (\text{s12})$$

## S3.2 Metasurface design

The goal of the system composed by the metasurface and the lens is to create a focused beam of light hosting the complete polarization singularity at its focal point. The key idea is to use the Green's function approach to compute the contribution of each region of the metasurface to the electric field in the focal point of the lens and in its neighborhood. This can be done analytically using a few assumptions about the system, which are satisfied by the experimental system. First, we will use the paraxial approximation to describe the beam after the lens. Second, all the focusing is performed by the lens, while the metasurface simply implements the required phase and polarization profile. It is possible to show that using a lossless metasurfaces based on rectangular pillars it is always possible to obtain a desired transmitted polarization and phase (represented by a Jones vector) given an input polarization and phase (40). In short, this is because any polarization can be converted to another by a proper wave plate, and an additional global delay can control the phase. In practice, the coverage is usually slightly lower than 100%, but this does not affect the formation of the singularity thanks to the fact that it is topologically protected.

At the focal point of the lens, we can deduce that the electric field is given by the integral of all the fields contributions over the metasurface area. To ensure that the field is zero, we design the metasurface to produce pairs of polarizations with opposite signs (phase shift of  $\pi$ ), so that all contributions sum to zero at the focal point (Fig S4A). Away from the focal point, the sum is not vanishing because of the additional phase delays introduced by the offset in the position. This idea is used routinely in other applications requiring 3D holography, including the generation of deexcitation beams for superresolution STED (57) and is summarized here.

- An offset  $dx$  with respect to the focal point is equivalent to a phase advance of the left side of the metasurface and a phase delay on the right side (or vice versa), Fig S4B.
- An offset  $dy$  with respect to the focal point is equivalent to a phase advance of the top side of the metasurface and a phase delay on the bottom side (or vice versa), Fig S4C.
- An offset  $dz$  is equivalent to a certain phase delay (or advance) in the center of the metasurface and a smaller phase delay (or advance) on the rim of the metasurface. Normalizing all fields with the average phase (which can always be done without affecting the continuity of the fields), this is equivalent to a phase advance at the center of the metasurface and a phase delay on the rim (or vice versa), Fig S4D.

Because the target polarization and phase around the singularity is  $|\psi\rangle = (dx + idy)|H\rangle + dz|V\rangle$  this is equivalent to mapping the vertical polarization at the center ( $r = 0$ ) and at the rim ( $r = r_0$ ) of the metasurface, and the horizontal polarization in a circle at  $r = \sqrt{0.5}r_0$ . This factor is chosen to ensure that the rim region ( $r > \sqrt{0.5}r_0$ ) has the same area of the center region ( $r < \sqrt{0.5}r_0$ ) to balance the sum to 0 at the focal point. Additionally, an OAM-like azimuthal phase profile has to be imparted on the horizontal polarization.

These considerations provide the ansatz that the mapping can be performed in a one-to-one manner from the metasurface to the region of space around the focal point (Fig S4E), choosing the desired Jones vector to be:

$$\begin{pmatrix} E_x \\ E_y \end{pmatrix} = e^{i\phi_0+i\theta} \begin{pmatrix} \cos\left(\frac{\pi r}{r_0}\right)^{2+\varepsilon} \\ \sin\left(\frac{\pi r}{r_0}\right)^{2+\varepsilon} \end{pmatrix} \quad (\text{S13})$$

where  $r, \theta$  are the polar coordinates on the metasurface,  $r_0$  is the radius of the metasurface,  $\phi_0$  is a global phase factor and  $\varepsilon$  is a small correction to the exponent. The ansatz is then validated by the simulations, which show that the desired profile is obtained around the focal point

To ensure the correct behavior with the wavelength, several free parameters were used:

- The input polarization
- The correction  $\varepsilon$
- The global phase.

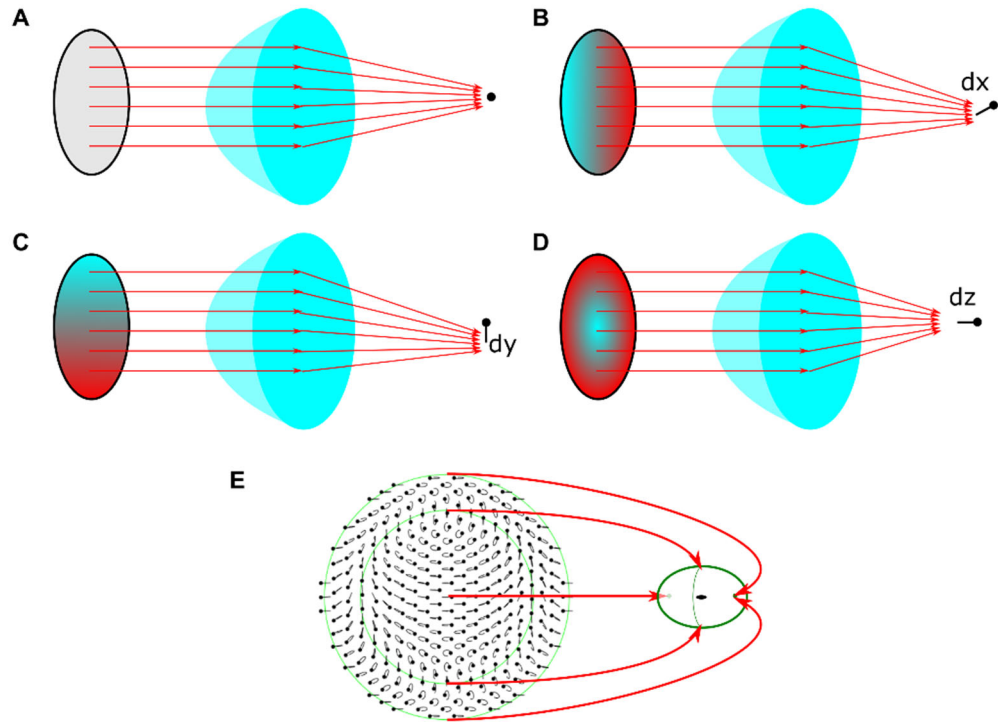


**Figure S5: Design of the phase and polarization profile.** A, at the focal point the intensity of light is zero because polarizations cancel each other in pair. B-D, offsets in the 3D space are equivalent to additional phase gradients on the metasurface. E, mapping from the metasurface to the fields around the singularity.

### S3.3 Metasurface library simulation and metasurface implementation

The design principle of using rotated rectangular pillars to fully control phase and polarization of light is described in (40). The metasurface library is composed of rectangular pillars of height  $L_z = 600\text{nm}$  and varying length and width and is depicted in Figure S6. The unit cell size was chosen to be  $U_x = U_y = 420\text{nm}$ . The phase delay of the meta atom was simulated using the RCWA-software Reticolo (55), assuming  $n_{\text{SiO}_2} = 1.46$  and  $n_{\text{TiO}_2} = 2.4$ .

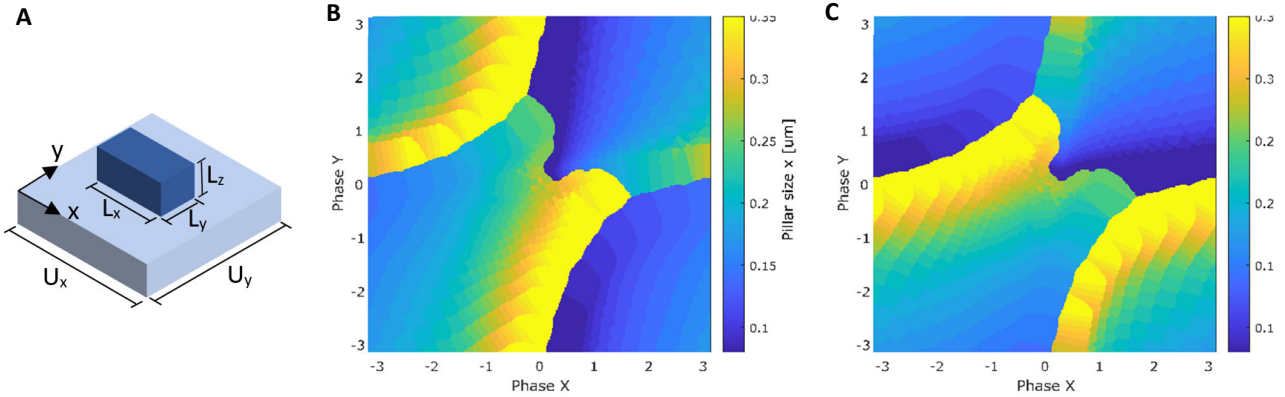


**Figure S6: Metasurface pillar library.** **a**, Depiction of a unit cell design. A rectangular  $\text{TiO}_2$  pillar ( $n_{\text{TiO}_2} = 2.4$ ) of varying length and width but constant height  $L_z = 600\text{nm}$  is placed in the center of a unit cell of dimension  $U_x = 420\text{nm}$ ,  $U_y = 420\text{nm}$ . The horizontally polarized light ( $E_x$ ) impinges from the side of the  $\text{SiO}_2$  substrate ( $n_{\text{SiO}_2} = 1.46$ , simulated as semi-infinite). **b**, Direction dependent phase delay for a single wavelength (600nm) vs Pillar dimension  $L_y$ . **c**, Direction dependent phase delay for a single wavelength (600nm) vs Pillar dimension  $L_x$ .

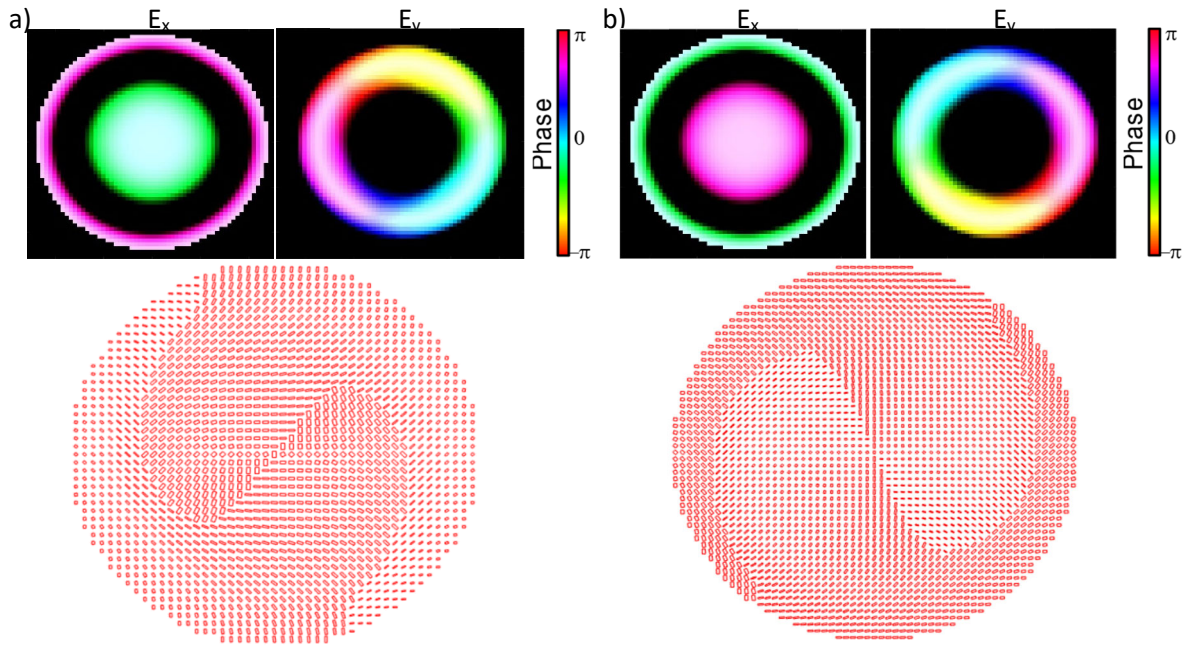


**Figure S7: Metasurface implementation and global phase.** Schematic of the metasurface implementation, sampling every 25th pillar. **a**, metasurface used for the experiment with global phase  $\phi_{global} = -0.25\pi$ . **b**, same phase profile implementation, but with global phase  $\phi_{global} = 0.75\pi$ , that implements the same polarization, but changes the selection of pillars.

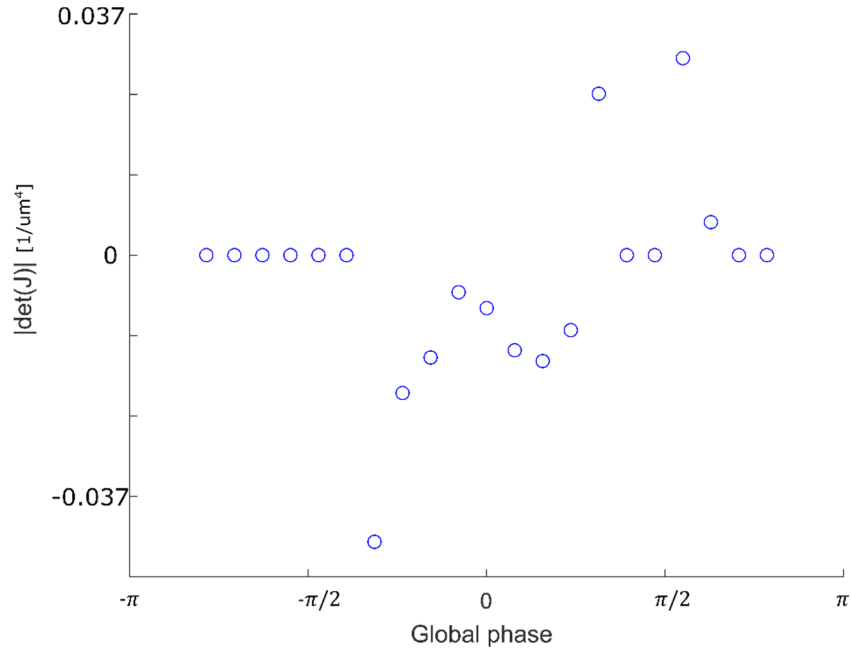


**Figure S8. Influence of the global phase on the Jacobian.** Global phase against the Jacobian determinant at the position of the singularity, showing that the global phase can control the wavelength confinement and can be used to ensure  $|\det(J)| > 0$ .

### S3.4 Simulation of the electric field

The field around the singularity is simulated using a green function integral:

$$\mathbf{E}(x_s, y_s, z_s, \lambda_s) \sim \iiint_{MS} dx dy dz \mathbf{T}_{MS}(x, y, z, \lambda) \underbrace{e^{-i\frac{2\pi}{\lambda_s} \sqrt{x^2 + y^2 + f_{lens}^2}}}_{\text{Aspheric lens}} \underbrace{e^{i\frac{2\pi}{\lambda_s} \sqrt{(x-x_s)^2 + (y-y_s)^2 + z_s^2}}}_{\text{Green function}} \quad (S14)$$

where  $f_{lens} = 3.1\text{mm}$  is the focal length of the aspheric lens and  $\mathbf{T}_{MS}$  corresponds to the complex transmission right after the metasurface sampled with nanostructures from the library described in S3.2. Note that the Green's function is approximated by discarding the inverse square of the radius decay, which has negligible variation. To reduce computation time, the metasurface was assumed to be ten times smaller than the true size. However, this does not change the resulting normalized field distribution, and it was verified using different scaling values and always obtaining the same results. As the metasurface and the aspheric lens are placed close together, the diffraction effects from the metasurface edges are neglected. To simulate the effect of a perturbation shadowing part of the metasurface, the corresponding part of the metasurfaces transmission profile is set to zero.

As the phase profile of the sampled metasurface does not perfectly match the ideal phase profile (Figure 2c), the singularity will not be placed perfectly at the design position  $(x_0, y_0, z_0, \lambda_0) = (0, 0, 3.1\text{mm}, 600\text{nm})$ , but will be slightly displaced in 4D space even in the simulation. We hence use a root finding algorithm to find the singularity. Specifically, we use the iterative Newton Raphson algorithm following:

$$u_{n+1} = u_n - f(u_n) * J^{-1}(u_n)$$

with  $u_n = (x_n, y_n, z_n, \lambda_n)$  being the position in 4D space for the nth step,  $f(u_n)$  being the complex field value at position  $u_n$  and  $J^{-1}(u_n)$  being the inverted Jacobian at position  $u_n$ . Starting from different positions around the design position, we see a convergence to the singularity that is indeed shifted in the 4D space (Figure S10).

This algorithm also ensures that the simulated singularity is a first order and not a higher order zero in four dimensions. Choosing the starting position  $u_0$  randomly around the found singularity, we can observe its convergence behaviour (Figure S9). While this algorithm converges for first order zeros, it would not converge for higher order zeros as  $J^{-1}$  diverges in at least one entry the closer the walker gets to higher order zeros. When divergence occurs, the sequence of points jumps chaotically instead of converging, and it is worth mentioning that the Newton's fractal is related to the convergence/divergence pattern of this algorithm.

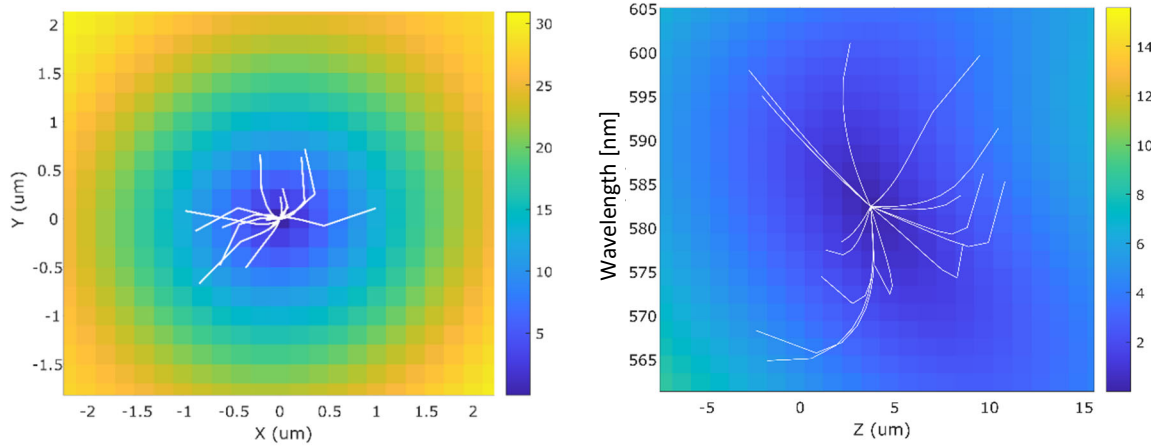


**Figure S9. Finding the singularity using the Newton Raphson algorithm.** The paths converge to the true singularity position.

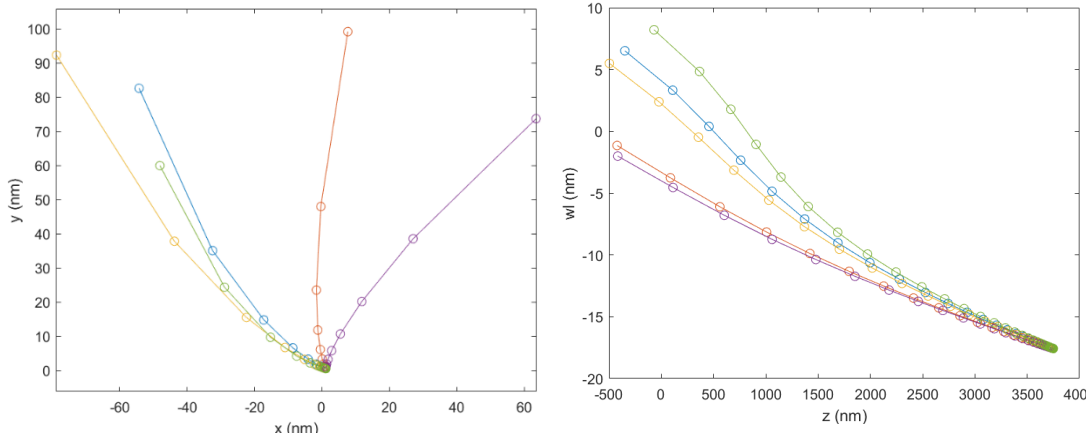


**Figure S10. Validation of singularities in 4D: The Newton Raphson algorithm.** Simulations show a singularity in space and wavelength with trajectories (white) of the Newton-Raphson method.

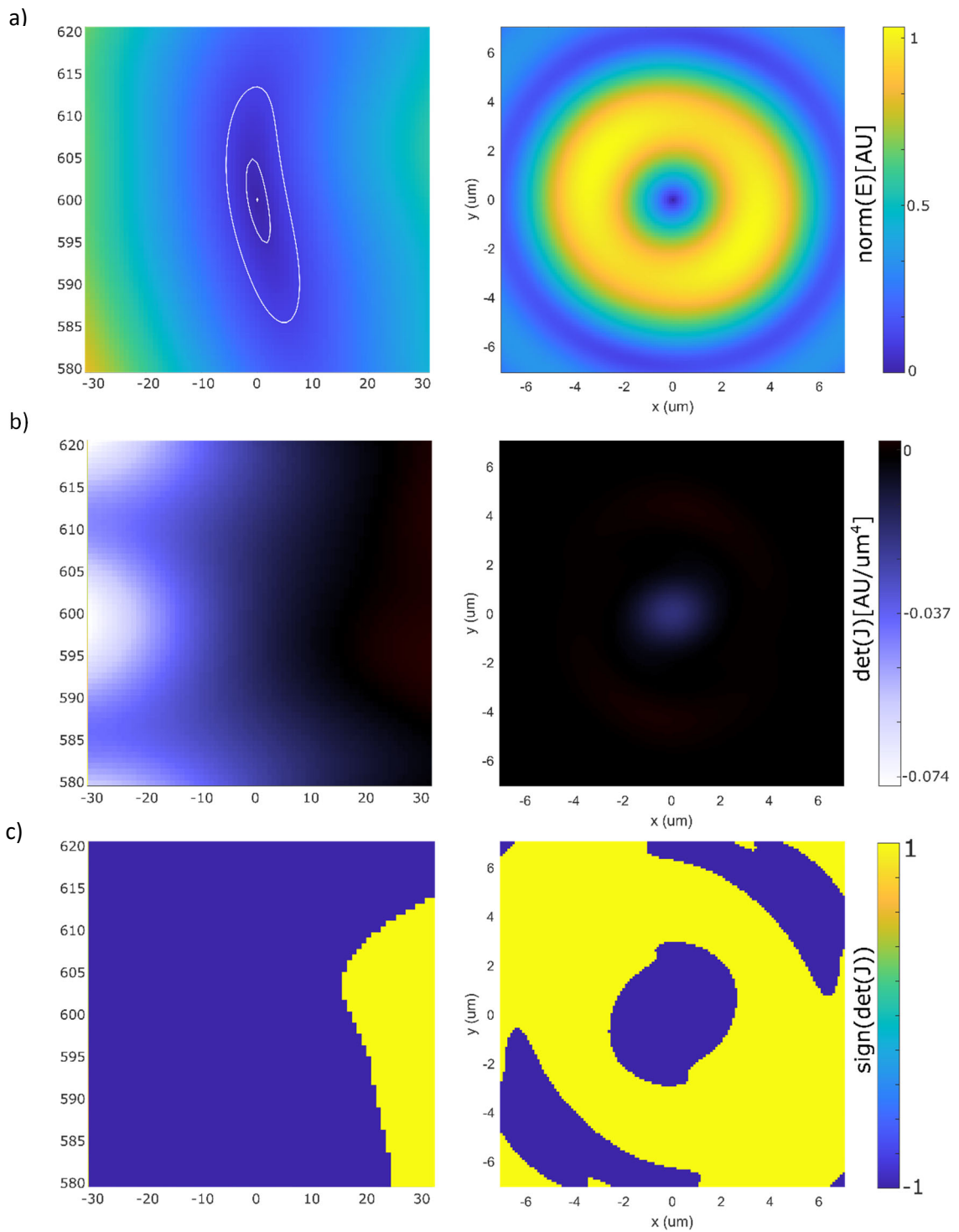


**Figure S11. Validation of complete polarization singularities: Calculating the Jacobian.** **a**, normalized field around the singularity in 4D. **b**, corresponding Jacobian determinant in 4D showing that the singularity is positioned in a region of negative Jacobian hence  $m_{4D} = \text{sign}(\det(\bar{J})) = -1$ . **c**, corresponding sign of the Jacobian determinant.

#### **S4 Metasurface fabrication details**

To ensure that light can only pass through the metasurface and is blocked otherwise, the metasurface is fabricated into an open aperture of an Aluminum mask. The steps for the mask fabrication are summarized in Supplementary Figure S12. To define the position of the hole and the alignment markers, LOR3A and S1813 resist were spin coated on a glass substrate, exposed with optical lithography (maskless aligner) and developed with MF319. 150nm of Al were then deposited in a vacuum E-beam Evaporator and the resist was removed using Remover PG at 80 C. The same procedure was repeated using 50nm of gold to make the alignment markers visible in the electron beam lithography for the following metasurface writing. The diameter of the gold mask hole was chosen to be larger than the metasurface as it would further increase the resist height close to the mask boundary due to capillary forces and hence complicate the metasurface fabrication.

Supplementary Figure S13 depicts the subsequent metasurface fabrication in the center of the mask opening. 600nm of ZEP resist were spin coated onto the mask, exposed with electron beam lithography, and developed with cold o-xylene. TiO<sub>2</sub> was deposited via ALD on the patterned resist, and the excess oxide was etched back using a fluorine based RIE recipe. The resist was removed in Remover PG at 80 C. The sample was rinsed in acetone, IPA, and cleaned using oxygen plasma.

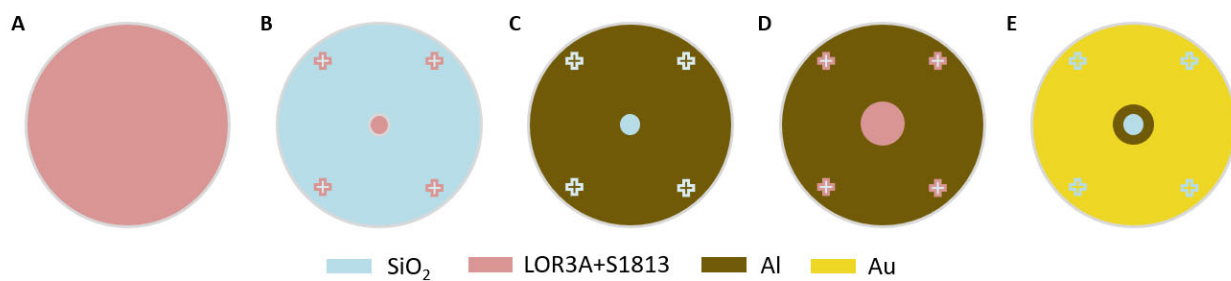


**Figure S12. Aluminium and gold mask fabrication.** **a**, Spin coating optical lithography resist. **b**, Optical lithography exposure and development freeing everything but alignment markers and the final hole of the mask. **c**, Al deposition using Vacuum E-beam Evaporator and lift-off in remover PG. **d**, Spin coating optical lithography resist, optical lithography exposure and development freeing everything but alignment markers and a region larger than the initial hole in the Al mask. **e**, Gold deposition using Vacuum E-beam Evaporator and lift-off in remover PG.

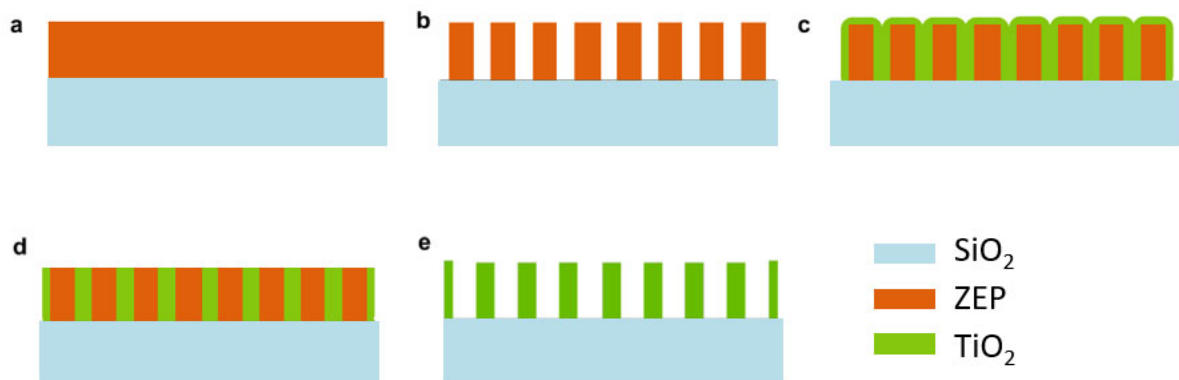


**Figure S13. Metasurface fabrication.** **a**, Spin coating e-beam resist. **b**, e-beam exposure and development. **c**, TiO<sub>2</sub> deposition using ALD. **d**, RIE etch back. **e**, Resist removal and final cleaning.

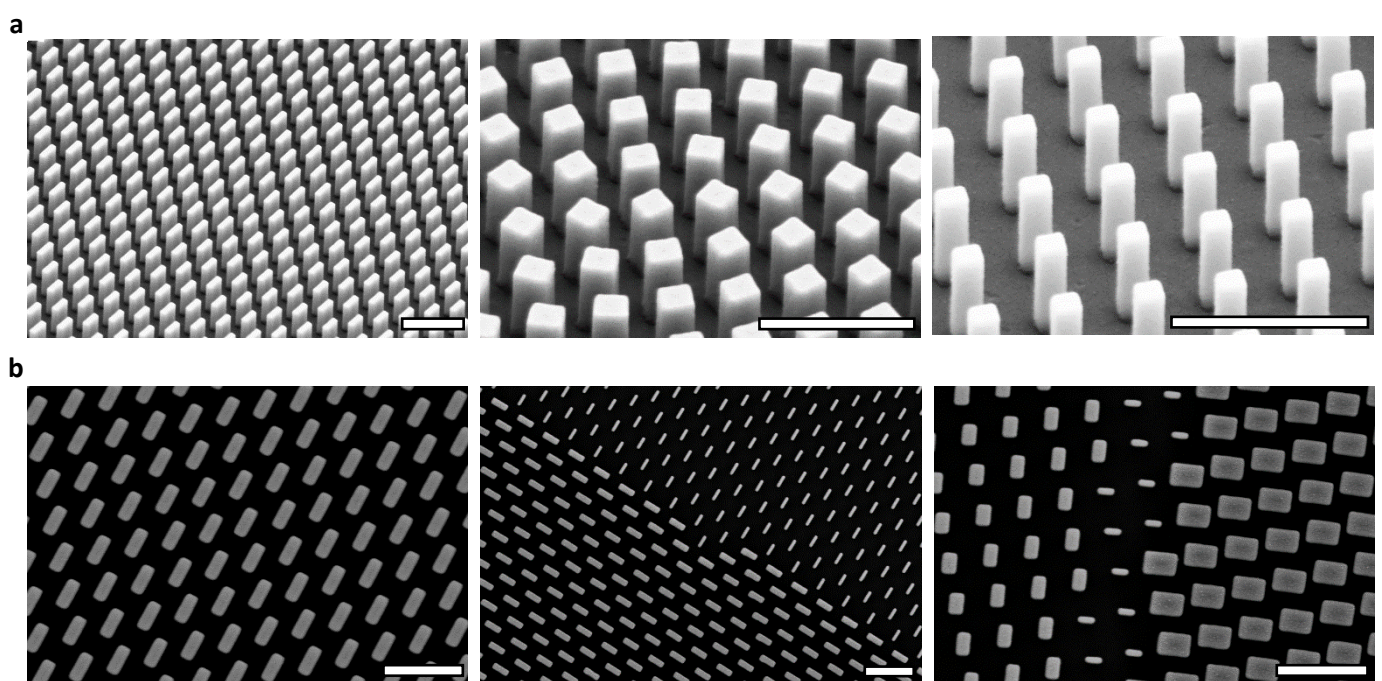


**Figure S14. SEM images of the fabricated metasurface.** **a**, Different regions of the metasurface. Images taken under an 40° angle. Scale bar 1 $\mu$ m. **b**, Different regions of the metasurface (top view). Scale bar 1 $\mu$ m.

## S5 Measurement details

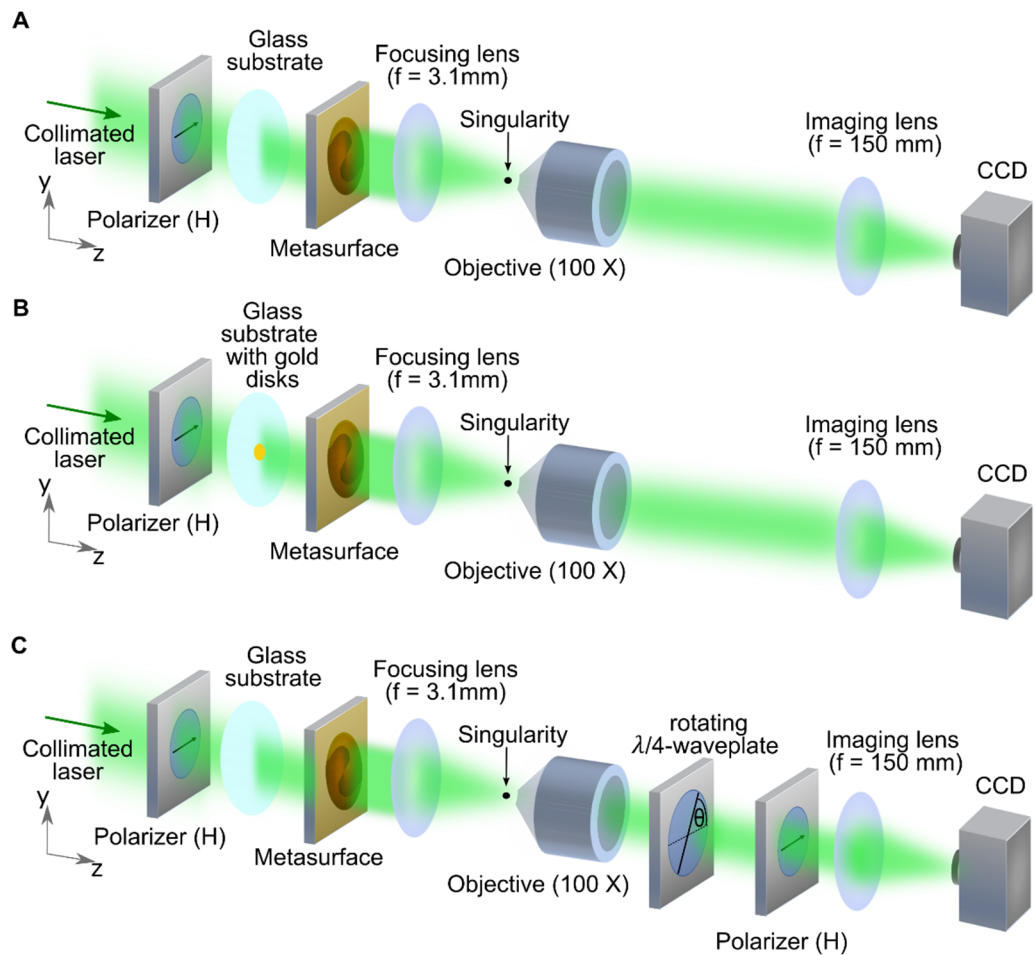


**Figure S15. Measurement setup.** **a**, Setup for intensity measurements. A collimated laser beam of adjustable wavelength is generated by a supercontinuum laser with a reconfigurable bandpass filter of 5 nm bandwidth and then passing through a horizontal polarizer and a glass substrate (to exclude effects from the glass substrate holding the perturbation gold disk in b)) before passing through the metasurface ( $500\mu m$ ). Light impinging outside of the metasurface area is blocked by a Al/Au mask. An aspheric lens of  $f=3.1mm$  (NA 0.08) is then used to focus the light and create the singularity. The singularity is then imaged with a microscope formed by an 100x objective (Nikon, NA=0.9), an imaging lens of  $f=15cm$  and a sCMOS camera (color sensor, pixel size  $6.5\mu mx6.5\mu m$ , dynamic range 21500:1) A motorized stage is used to move the objective along the z-direction. The metasurface, the glass substrate and the focusing lens are positioned on 3-axis stages with micrometer heads to enable precise positioning. **b**, Setup for perturbation measurements. The setup is identical to a) except that this time a gold disk on the glass substrate is moved in front of the metasurface to block part of the metasurface. **c**, Setup for polarization measurements. Measurement setup is identical to a), except that a quarter-waveplate (mounted on a motorized rotation stage) and a horizontal polarizer is added into the infinity space between the objective and the imaging lens.

## **S5.1 Intensity measurement and data analysis**

### **S5.1.1 Intensity measurement and data analysis**

A detailed setup description can be found in Figure S15 a. As the camera captures slices of the field in the xy plane, additional sweeps in wavelength and z position were performed in order to capture the field around the singularity in the 4D space ( $x, y, z, \lambda$ ). The resolution of the sweep is: ( $\Delta x, \Delta y, \Delta z, \Delta \lambda$ )=( $0.17\mu\text{m}, 0.17\mu\text{m}, 2\mu\text{m}, 2\text{nm}$ ). Subsequently, the laser was turned off, 1000 background images were captured and the pixel-wise average was subtracted from the captured images to compensate for stray light from the room directly hitting the sCMOS. To compensate for laser power differences between different wavelengths, the captured images were normalized by the total pixel count (the area of capture is chosen large enough to capture all light passing from the laser through the system (Figure S15)). One remaining source of error is the finite bandwidth of the laser (5nm), that is larger than the wavelength steps of the measurement and hence increase the intensity at the singularity position.

#### Finding the singularity position in four dimensions:

To find the position of the singularity in the four-dimensional space, we loop through the positions in z and wavelength and search in each xy slice for the minimum intensity inside the circle of light (Figure S16 a). Due to the circular shape of the field surrounding the singularity, a weighted average of the image (excluding pixels smaller than the maximum pixel of the background image) gives a first estimate of the singularity position (Figure S16b). The minimum and its position can then be found by reducing the area of interest to an area inside of the light ball around the estimated position (Figure S16c). A repeating reduction in area of interest and updating of the estimation point then converges to the position of interest. The singularity position is determined by iterating these procedures for all position in z and wavelength, searching for the position  $v = (x_0, y_0, z_0, \lambda_0)$  where the intensity of the point of interest within the circle of light is minimized.

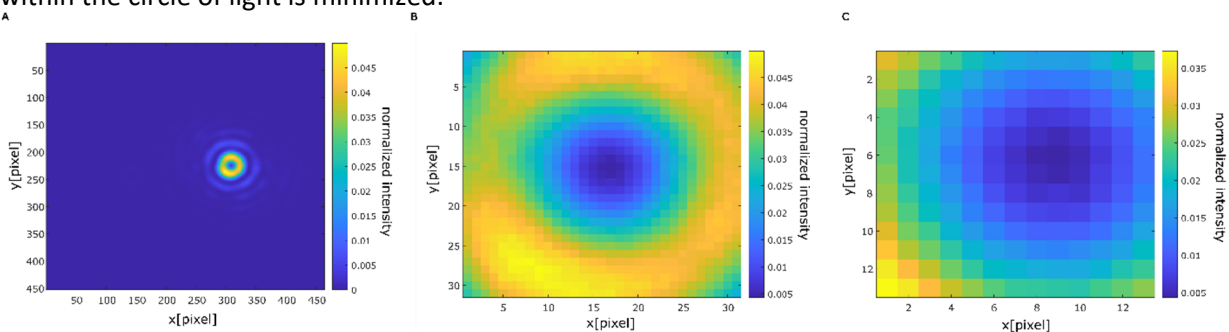


**Figure S16. Finding the singularity.** **a**, xy slice captured by the sCMOS camera, normalized by the total pixel count to compensate for wavelength dependent power changes. **b**, First reduced area of interest centred at the weighted average position. **c**, Reduced area of interest. The minimum field value is taken from this picture.

xy confinement (Figure 3c): The xy slice is plotted at  $z = z_0$  and  $\lambda = \lambda_0$  using the dB scale with  $I_{dB} = 10 \log_{10}(I/I_{max})$ , where  $I$  is the intensity of the xy slice and  $I_{max}$  is the maximum intensity value in the four dimensional space of the captured data (after compensation for laser power difference between different wavelength). The dB scale is chosen, to better represent the range of fields close to the singularity.

$z\lambda$  confinement (Figure 3d). For each position in z and wavelength, the corresponding xy-slice is processed like Figure 3c) and the intensity of the minimal point within the circle of light is plotted.

xyz confinement (Figure 3e). The data was represented in dB, with  $I_{max}$  being the maximum value in the whole four-dimensional dataset.

## **S5.2 Perturbation measurement and data analysis**

To experimentally demonstrate the perturbation protection of the singularity, we insert an opaque gold disk of diameter of  $110 \mu m$  in front of the metasurface, blocking part of the light from passing through. Due to the way the metasurface converts light into different polarizations over different areas of the metasurface, this corresponds to subtracting a polarized field in comparison to the unperturbed singularity. A detailed setup description can be found in Figure S15b. As the glass substrate holding the gold disk perturbation was added already in the unperturbed measurement (the gold mask was pushed out of the metasurface area), we can ensure that the perturbation effects are not caused by the glass substrate. The data analysis is described in S5.1.

## **S5.3 Polarization measurement and data analysis**

To analyze the polarization of the field around the singularity, we follow the mechanism described in (48). Adding a quarter waveplate and a horizontal polarizer to the infinity space between the objective and the imaging lens, one can retrieve the full Stokes vector at each pixel in the xy slice by rotating the quarter waveplate and capturing images at multiple angles  $\theta$  (example measurement shown in Figure S17 left side):

$$\begin{aligned} A &= \frac{2}{N} \sum_{n=1}^N I_n, & B &= \frac{4}{N} \sum_{n=1}^N I_n \sin 2\theta_n \\ C &= \frac{4}{N} \sum_{n=1}^N I_n \cos (4\theta_n), & D &= \frac{4}{N} \sum_{n=1}^N I_n \sin 4\theta_n \end{aligned} \quad (S15)$$

Where  $\theta_{n+1} - \theta_n = 180^\circ/N$ . The Stokes parameters then are determined by

$$S_0 = A - C, \quad S_1 = 2C, \quad S_2 = 2D, \quad S_3 = B \quad (S16)$$

This procedure is repeated in a z region of  $\pm 10 \mu m$  around the singularity (stepsize  $4 \mu m$ ). Figure 3G in the main paper is created by evaluating the stokes vector on an elliptical surface of constant intensity around the singularity position with  $\lambda = \lambda_0$  and polar plotting the corresponding polarization ellipse at position  $(\rho, \phi)$  with

$$\rho = \text{atan2}((x - x_{\text{centre}}), (y - y_{\text{centre}})), \quad \phi = |\text{atan}(\frac{\sqrt{(x - x_{\text{centre}})^2 + (y - y_{\text{centre}})^2}}{z})| \quad (S17)$$

, where  $(x_{\text{centre}}, y_{\text{centre}})$  is the singularity position. Each pixelated data ring of each xy slice (Figure S18b) is projected onto a perfect ring of radius  $R = \frac{\sum_i^N \sqrt{(x_i)^2 + (y_i)^2}}{N}$  for representation reasons.

Figures S17 and S18 show other representations of the measured polarizations. Figure S15b shows a comparison between the experimental and simulated stokes vectors in the xy plane at  $z = z_0$  and  $\lambda = \lambda_0$ , showing a good agreement. S18c,d show that the measured polarization states around the singularity cover the entire Poincare sphere, with an uneven distribution of datapoints due to the finite pixel size of the sCMOS camera (Figure S18 a,b).

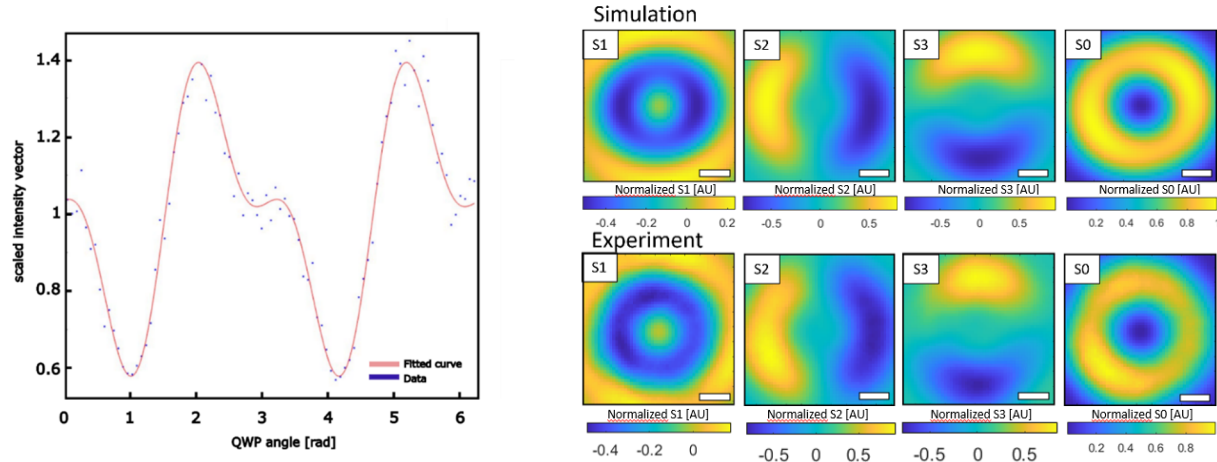


**Figure S17. Stokes vector extraction.** a, The intensity changes of a pixel depending on the rotation angle of the quarter waveplate (QWP) with respect to the horizontal polarizer. It can be used to extract the Stokes vector following the algorithm described in (48). b, Simulated (top) vs. experimental (bottom) stokes vector components. Scale bar 2um.

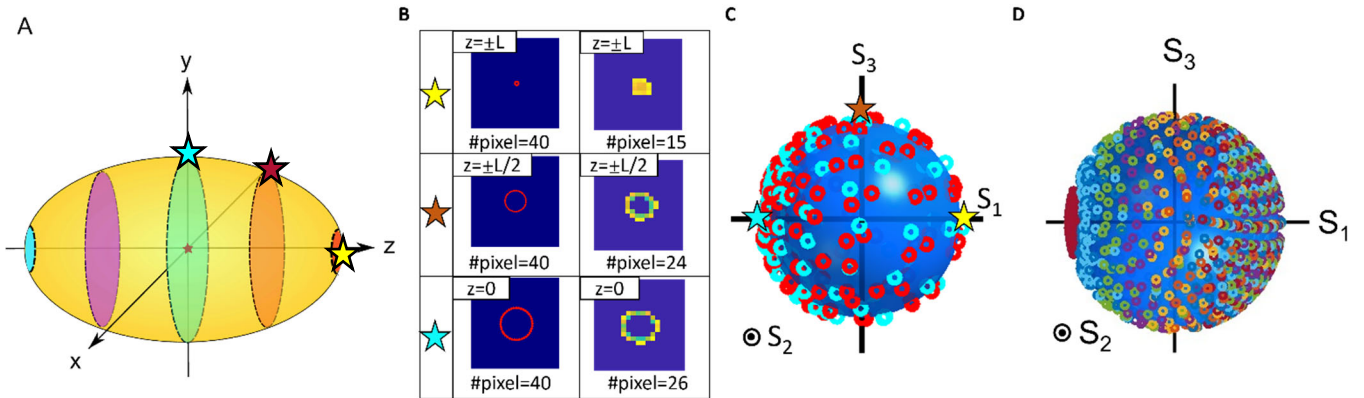


**Figure S18. Simulated and experimental polarization plotted on Poincare sphere.** a, Schematic of an ellipsoid around the singularity position (star in the origin) of equal intensity. xy-planes located at different z positions are marked in different colors, assuming the singularity is positioned at  $(x, y, z, \lambda) = (0, 0, 0, \lambda_0)$ . Stars mark different z positions for later comparison. b, Comparison of the number of datapoints available for different positions on the ellipsoid spheres for simulation (left) and experimental (right). The stars connect the position on the ellipsoid with the number of datapoints. While for the simulation the number of points on the ellipsoid is the same for each z position, the experimental data varies in datapoints due to the finite pixel size of the sCMOS camera. c, Due to the way the polarization is distributed on the

ellipsoid (see Figure S4), many datapoints are available for  $S_1=-1$  (as positioned on ellipsoid at  $z=0$ ), but only few datapoints are available for  $S_1=1$  (positioned on pole of ellipsoid at  $z=\pm z_{\max}$ ) causing a discrepancy of available datapoints between the left and right side of the Poincare sphere. Blue and red dots correspond to  $z>0$  and  $z<0$ , respectively. **d**, Same as for c), with increased ellipsoid size. Different colors correspond to different  $z$  positions on the ellipsoid, showing that indeed different  $z$  positions on the ellipsoid correspond to different positions on the  $S_1$  axis on the Poincare sphere.

## REFERENCES AND NOTES

1. G. J. Gbur, *Singular Optics* (CRC Press, 2016).
2. J. F. Nye, M. V. Berry, Dislocations in wave trains, in *A Half-Century of Physical Asymptotics and Other Diversions: Selected Works by Michael Berry* (World Scientific, 2017), pp. 6–31.
3. M. Soskin, S. V. Boriskina, Y. Chong, M. R. Dennis, A. Desyatnikov, Singular optics and topological photonics. *J. Opt.* **19**, 10401 (2016).
4. M. R. Dennis, K. O'holleran, M. J. Padgett, Singular optics: Optical vortices and polarization singularities, in *Progress in Optics* (Elsevier, 2009), vol. 53, pp. 293–363.
5. W. Whewell, Singular optics: More ado about nothing. *J. Opt. A: Pure Appl. Opt.* **11**, 090201 (2009).
6. A. S. Desyatnikov, Y. S. Kivshar, L. Torner, Chapter 5—Optical vortices and vortex solitons, in *Progress in Optics*, E. Wolf, Ed. (Elsevier, 2005), vol. 47, pp. 291–391.
7. M. V. Berry, Geometry of phase and polarization singularities illustrated by edge diffraction and the tides, in *Second International Conference on Singular Optics (Optical Vortices): Fundamentals and Applications* (Bellingham Washington, 2001), vol. 4403, pp. 1–12.
8. W. Liu, W. Liu, L. Shi, Y. Kivshar, Topological polarization singularities in metaphotonics. *Nanophotonics* **10**, 1469–1486 (2021).
9. Y. Shen, X. Wang, Z. Xie, C. Min, X. Fu, Q. Liu, M. Gong, X. Yuan, Optical vortices 30 years on: OAM manipulation from topological charge to multiple singularities. *Light Sci. Appl.* **8**, 90 (2019).
10. H. Rubinsztein-Dunlop, A. Forbes, M. V. Berry, M. R. Dennis, D. L. Andrews, M. Mansuripur, C. Denz, C. Alpmann, P. Banzer, T. Bauer, Roadmap on structured light. *J. Opt.* **19**, 13001 (2016).

11. A. H. Dorrah, F. Capasso, Tunable structured light with flat optics. *Science* **376**, eabi6860 (2022).
12. M. Vasnetsov, *Optical Vortices* (Nova Science Pub Incorporated, 1999), vol. 228.
13. M. V. Berry, M. R. Dennis, Phase singularities in isotropic random waves. *Proc. Math. Phys. Eng. Sci.* **456**, 2059–2079 (2000).
14. Q. Zhan, Cylindrical vector beams: From mathematical concepts to applications. *Adv. Opt. Photonics* **1**, 1–57 (2009).
15. J. F. Nye, Monstars on glaciers. *J. Glaciol.* **29**, 70–77 (1983).
16. J. F. Nye, *Natural Focusing and Fine Structure of Light: Caustics and Wave Dislocations* (CRC Press, 2000).
17. J. F. Nye, Lines of circular polarization in electromagnetic wave fields. *Proc. R. Soc. A Math. Phys. Sci.* **389**, 279–290 (1983).
18. J. F. Nye, J. V. Hajnal, The wave structure of monochromatic electromagnetic radiation. *Proc. R. Soc. A Math. Phys. Sci.* **409**, 21–36 (1987).
19. J. V. Hajnal, Singularities in the transverse fields of electromagnetic waves I. Theory. *Proc. R. Soc. A Math. Phys. Sci.* **414**, 433–446 (1987).
20. M. V. Berry, M. R. Dennis, Polarization singularities in isotropic random vector waves. *Proc. Math. Phys. Eng. Sci.* **457**, 141–155 (2001).
21. E. J. Galvez, Light beams with spatially variable polarization. *Photonics: Scientific Foundations, Technology and Applications* **1**, 61–76 (2015).
22. M. R. Dennis, Polarization singularities in paraxial vector fields: Morphology and statistics. *Opt. Commun.* **213**, 201–221 (2002).

23. D. Susic, R. Droop, E. Otte, D. Ehrmanntraut, F. Nori, J. Ruostekoski, C. Denz, M. R. Dennis, Particle-like topologies in light. *Nat. Commun.* **12**, 6785 (2021).
24. S. W. D. Lim, J.-S. Park, M. L. Meretska, A. H. Dorrah, F. Capasso, Engineering phase and polarization singularity sheets. *Nat. Commun.* **12**, 4190 (2021).
25. A. J. Vernon, F. J. Rodriguez-Fortuño, Creating and moving nanoantenna cold spots anywhere. *Light Sci. Appl.* **11**, 1–10 (2022).
26. L. Lu, J. D. Joannopoulos, M. Soljačić, Topological photonics. *Nat. Photonics* **8**, 821–829 (2014).
27. B. Zhen, C. W. Hsu, L. Lu, A. D. Stone, M. Soljačić, Topological nature of optical bound states in the continuum. *Phys. Rev. Lett.* **113**, 257401 (2014).
28. M. Kim, Z. Jacob, J. Rho, Recent advances in 2D, 3D and higher-order topological photonics. *Light Sci. Appl.* **9**, 130 (2020).
29. M. R. Dennis, H. H. Wills, thesis, University of Bristol, Bristol, UK (2001).
30. J. Gâteau, F. Claude, G. Tessier, M. Guillon, Topological transformations of speckles. *Optica* **6**, 914–920 (2019).
31. K. O'holleran, M. R. Dennis, M. J. Padgett, Topology of light's darkness. *Phys. Rev. Lett.* **102**, 143902 (2009).
32. J. W. Goodman, *Speckle Phenomena in Optics: Theory and Applications* (Roberts and Company Publishers, 2007).
33. L. Yuan, Q. Lin, M. Xiao, S. Fan, Synthetic dimension in photonics. *Optica* **5**, 1396–1405 (2018).
34. A. F. Beardon, *Complex Analysis: The Argument Principle in Analysis and Topology* (Courier Dover Publications, 2019).

35. I. V Basistiy, V. Y. Bazhenov, M. S. Soskin, M. V. Vasnetsov, Optics of light beams with screw dislocations. *Opt. Commun.* **103**, 422–428 (1993).
36. G. Fonseca, I. Fonseca, W. Gangbo, in *Degree Theory in Analysis and Applications* (Oxford Univ. Press, 1995), vol. 2.
37. M. Born, E. Wolf, *Principles of Optics: Electromagnetic Theory of Propagation, Interference and Diffraction of Light* (Elsevier, 2013).
38. A. S. Schwarz, *Topology for Physicists* (Springer Science & Business Media, 2013), vol. 308.
39. K. Tekce, E. Otte, C. Denz, Optical singularities and Möbius strip arrays in tailored non-paraxial light fields. *Opt. Express* **27**, 29685–29696 (2019).
40. J. P. B. Mueller, N. A. Rubin, R. C. Devlin, B. Groever, F. Capasso, Metasurface polarization optics: Independent phase control of arbitrary orthogonal states of polarization. *Phys. Rev. Lett.* **118**, 113901 (2017).
41. N. A. Rubin, Z. Shi, F. Capasso, Polarization in diffractive optics and metasurfaces. *Adv. Opt. Photonics* **13**, 836–970 (2021).
42. B. Harke, C. K. Ullal, J. Keller, S. W. Hell, Three-dimensional nanoscopy of colloidal crystals. *Nano Lett.* **8**, 1309–1313 (2008).
43. N. A. Rubin, G. D’Aversa, P. Chevalier, Z. Shi, W. T. Chen, F. Capasso, Matrix fourier optics enables a compact full-stokes polarization camera. *Science* **365**, eaax1839 (2019).
44. A. Zaidi, N. A. Rubin, A. H. Dorrah, J.-S. Park, F. Capasso, Generalized polarization transformations with metasurfaces. *Opt. Express* **29**, 39065–39078 (2021).
45. W. T. Chen, A. Y. Zhu, F. Capasso, Flat optics with dispersion-engineered metasurfaces. *Nat. Rev. Mater.* **5**, 604–620 (2020).

46. M. Khorasaninejad, W. T. Chen, R. C. Devlin, J. Oh, A. Y. Zhu, F. Capasso, Metalenses at visible wavelengths: Diffraction-limited focusing and subwavelength resolution imaging. *Science* **352**, 1190–1194 (2016).
47. R. C. Devlin, M. Khorasaninejad, W. T. Chen, J. Oh, F. Capasso, Broadband high-efficiency dielectric metasurfaces for the visible spectrum. *Proc. Natl. Acad. Sci. U.S.A.* **113**, 10473–10478 (2016).
48. B. Schaefer, E. Collett, R. Smyth, D. Barrett, B. Fraher, Measuring the Stokes polarization parameters. *Am. J. Phys.* **75**, 163–168 (2007).
49. H. Wolter, Concerning the path of light upon total reflection. *J. Opt. A Pure Appl. Opt.* **11**, 090401 (2009).
50. G. H. Yuan, N. I. Zheludev, Detecting nanometric displacements with optical ruler metrology. *Science* **364**, 771–775 (2019).
51. E. Langereis, S. B. S. Heil, M. C. M. van de Sanden, W. M. M. Kessels, In situ spectroscopic ellipsometry study on the growth of ultrathin TiN films by plasma-assisted atomic layer deposition. *J. Appl. Phys.* **100**, 023534 (2006).
52. J. Linke, J. Du, T. Loewenhoff, G. Pintsuk, B. Spilker, I. Steudel, M. Wirtz, Challenges for plasma-facing components in nuclear fusion. *Matter Radiat. Extremes* **4**, 056201 (2019).
53. U. V. Nägerl, T. Bonhoeffer, Imaging living synapses at the nanoscale by STED microscopy. *J. Neurosci.* **30**, 9341–9346 (2010).
54. Z. Shi, A. Y. Zhu, Z. Li, Y.-W. Huang, W. T. Chen, C.-W. Qiu, F. Capasso, Continuous angle-tunable birefringence with freeform metasurfaces for arbitrary polarization conversion. *Sci. Adv.* **6**, eaba3367 (2020).
55. J. P. Hugonin, P. Lalanne, Reticolo software for grating analysis, preprint arXiv:2101.00901 (2021).

56. P. Senthilkumaran, S. K. Pal, Phase singularities to polarization singularities. *Int. J. Opt.* **2020**, 1–33 (2020).
57. S. W. Hell, J. Wichmann, Breaking the diffraction resolution limit by stimulated emission: Stimulated-emission-depletion fluorescence microscopy. *Opt. Lett.* **19**, 780–782 (1994).